PHYSICAL REVIEW B **99**, 125107 (2019)

First-principles calculations of photoluminescence and defect states of $\mathrm{Ce^{3+}}$-doped $\mathrm{(Ca/Sr)_2B_5O_9Cl}$

Jiajia Cai,[1,2] Weiguo Jing,[1] Jun Cheng,[1] Yongfan Zhang,[3] Yonghu Chen,[1] Min Yin,[1]
Yau-Yuen Yeung,[2,*] and Chang-Kui Duan[1,†]

[1]*Key Laboratory of Strongly-Coupled Quantum Matter Physics, Chinese Academy of Sciences, School of Physical Sciences, University of Science and Technology of China, Hefei 230026, People's Republic of China*
[2]*Department of Science and Environmental Studies, The Education University of Hong Kong, 10 Lo Ping Road, Tai Po, NT, Hong Kong, People's Republic of China*
[3]*Department of Chemistry, Fuzhou University, Fuzhou, Fujian 350002, People's Republic of China*

(Received 30 March 2018; published 7 March 2019)

Reliable predictions of electronic levels, excited-state geometric relaxation, and the relative energies of ground and excited levels to host band edges are of paramount importance for $\mathrm{Ce^{3+}}$-doped luminescent materials. By combining the constrained occupancy approach and the hybrid density functional calculation in the framework of a generalized Kohn-Sham formalism, we derived a calculation scheme for the band gap of the host material, the equilibrium configurations of ground-state $\mathrm{Ce^{3+}}$ and excited-state $\mathrm{(Ce^{3+})^*}$, and their relative energies with respect to host band edges in terms of hole capture or electron ionization for $\mathrm{Ce^{3+}}$ in $M_2\mathrm{B_5O_9Cl}$ ($M =$ Ca, Sr) charge compensated by $\mathrm{Na^+}$. The results of first-principles calculations for $4f \rightarrow 5d$ excitations, Stokes shifts, and the relative position of $5d$ levels to conduction-band edge agree well with experiments. The moderate computational cost of the present scheme, which can be applied in efficient prediction of the optical properties of many different Ce-doped materials, is of important value in screening potential lanthanide-doped scintillators and phosphors from minimal information about the host crystal structure.

DOI: 10.1103/PhysRevB.99.125107

I. INTRODUCTION

Cerium-doped inorganic compounds have received considerable attention because of their wide application in scintillators, light emitting diodes, and field emission displays [1–5]. The performance of the luminescent material is closely related to the position of the luminescent energy level in the band. For example, in the case of Ce-doped scintillators, the ground ($4f$) and excited ($5d$) states of $\mathrm{Ce^{3+}}$ need to reside in the band gap so as to trap a hole and then an electron sequentially (see Ref. [5] for more detailed discussions on scintillator mechanisms and quenching processes). An efficient and reliable calculation scheme is urgently needed for predicting the luminescent properties of various $\mathrm{Ce^{3+}}$-doped materials. Most of the first-principle calculations, which serve as powerful predictive tools in luminescent materials [6], are performed in either a quantum chemical method by utilizing cluster models or solid-state band-structural calculations based on supercells. The *ab initio* model potential (AIMP) embedded cluster model has been widely used to study properties such as excitations of F centers, spectroscopy of defects, luminescence, d-d excitations, and magnetic coupling constants [7–20]. This model has achieved reliable results which are in excellent agreement with experiments. However, it is fairly computationally demanding to incorporate the atomic relaxation of the excited state of luminescent material and to reconcile the localized multielectron levels of a cluster containing the impurity with those single quasiparticle band states of the host for an accurate description of luminescent processes. Based on density functional theory (DFT), calculation of the electronic structure of solids has emerged as a powerful approach for assessing the properties of defects with low computational complexity [21–23]. However, the traditional workhorse of DFT, the local-density approximation and generalized gradient approximation (GGA), often gives qualitatively incorrect behavior in cases such as when the electrons are nearly localized [24]. This problem, which is related to an overestimation of the delocalization in solids [25–27], can be eliminated or reduced in a fixed geometry calculation for the electron addition and electron removal energies by utilizing a many-body GW approximation [28–34]. However, the unfavorable scaling of the computational cost (in terms of both the computational time and the storage requirements) with respect to the system size, together with the complication of the convergence issue, are major challenges of GW approximation [28–34]. Alternatively, the inadequacies connected to the DFT treatment of localized states can be partially corrected in some limited cases by the DFT+U approach, where the parameter U can be determined either in an empirical way or in a self-consistent way from first-principles calculations [24,35–48]. The hybrid DFT approach that combines the elements of Hartree-Fock (HF) theory with DFT not only produces band structures that are in much better agreement with experiments compared to conventional DFT but also provides a much more reliable description of charge localization [49–57]. Perdew *et al.* [58] explains how the band edges and one-electron spectrum, obtained with meta-GGAs or hybrid functionals in the framework of generalized Kohn-Sham

---

[*] Corresponding author: yyyeung@eduhk.hk

[†] Corresponding author: ckduan@ustc.edu.cn

theory (GKS), are related to measured band gap and energies for a perfect crystal. Particularly, an excellent description of the one-electron spectrum related band gap for a perfect crystal has been given by GKS eigenvalues obtained with the hybrid Heyd-Scuseria-Ernzerhof 2006 (HSE06) function in both theory and practice [56–58]. Hence, we carry out the calculations by utilizing HSE06 with the HF mixing parameter $\alpha = 0.25$ and the screening parameter $\mu = 0.2$ as a compromise of computational efficiency and applicability. In addition, as a complement to the HSE06 calculation, a constrained occupancy approach [35–37] is adopted to calculate the equilibrium configuration of the excited $(Ce^{3+})^*$ state by setting the energy-ordered occupation numbers. As the same basis set and pseudopotential are used in ground-state and excited-state calculations, the calculated total energies and equilibrium configurations of the ground and excited states can be directly compared, and therefore the excitation and emission energies and the Stokes shift are obtained.

Ce^{3+} ion-doped $M_2B_5O_9Cl$ ($M =$ Ca, Sr) molecules are potential candidates for new neutron-imaging plates with possible applications in various fields such as neutron reflection and diffraction studies, small angle scattering, and tomography [59–63], because their low γ-ray sensitivity to neutron sensitivity ratio (about 2×10^{-2}) is favorable for reducing the γ-ray influence on the signal in the case when both neutrons and γ radiation take place. The wide band gap of the host together with the luminescent properties of Ce-doped $M_2B_5O_9Cl$ including all the five $5d$ levels and the Stokes shifts have been experimentally studied and well determined [59–63].

Hence, in this paper, we are dedicated to the prediction of the positions of $4f$ and $5d$ levels relative to the band edges in Ce-doped $M_2B_5O_9Cl$ by combining the hybrid HSE06 calculation and the constrained occupancy approach as a compromise between computational cost and accuracy. After having successfully applied the calculation scheme on such a specific luminescent material, we will discuss its further possible improvements and its applications in high-throughput predictions of luminescent properties of lanthanide-doped materials.

II. METHODOLOGY AND DETAILS

A. Geometric optimizations and band-structure calculations

The initial atomic positions and symmetry information of the host crystal were taken from the Inorganic Crystal Structure Database [64]. GGA–Perdew-Burke-Ernzerhof (PBE) calculations were adopted for atomic relaxation, as implemented in the Vienna *Ab Initio* Simulation Package (VASP) [65–69]. The primitive cell of $M_2B_5O_9Cl$ contains 17 atoms. A $2 \times 2 \times 2$ $M_2B_5O_9Cl$ supercell containing 136 atoms was chosen to model a pair of M cations substituted by a Ce-Na pair. The B ($2s^22p^1$), O ($2s^22p^4$), Na ($3s^1$), Cl ($3s^23p^5$), Ca ($3p^64s^2$), Sr ($4s^24p^65s^2$), and Ce ($5s^25p^64f^15d^16s^2$) were treated as valence electrons, and their interactions with the cores were described by the projector augmented wave method [70]. The structural relaxation was performed by utilizing the conjugate gradient technique. The equilibrium structures were obtained by optimizing atomic positions until the energy change was less than 10^{-6} eV and the Hellmann-Feynman forces on atoms were less than 0.01 eV/Å. The plane-wave cutoff energy was set to 550 eV and only one k-point Γ was used for sampling the Brillouin zone.

Band-structure calculations of the host $M_2B_5O_9Cl$ were carried out in VASP by utilizing fully self-consistent calculations with three k points centered at the Γ point following the Monkhorst-Pack scheme [71], and then 55 k points (including G, Z, T, Y, S, X, U, and R) were set to perform a non-self-consistent calculation to complete the band-structure calculations. Plane-wave cutoff energies were set at 550 and 400 eV for GGA-PBE and HSE06 calculations, respectively; the smaller cutoff energy was chosen for HSE06 as a compromise between computational cost and accuracy.

The band gaps of $M_2B_5O_9Cl$ were also calculated with the modified Becke-Johnson (mBJ) approach by utilizing the WIEN2K software package with the full-potential linearized augmented-plane-wave (FP-LAPW) method [72] for comparison with those calculated by utilizing the HSE06 functional in VASP, by considering that the mBJ approach based on a remarkably effective potential for exchange, as introduced by Becke and Johnson [73], has yielded an accurate description of the energy gap for various systems proposed by Tran and Blaha [74] and Koller *et al.* [75].

B. Constrained occupancy approach for excited-state geometry configuration

In order to obtain the Stokes shift, i.e., the difference between absorption and emission photon energies, we adopted a constrained occupancy approach for the equilibrium configuration of the excited state $(Ce^{3+})^*$ considering both the computational cost and accuracy. In practice, a constrained GGA calculation is performed by evacuating the seven spin-up predominantly Ce-$4f$ orbitals and filling the next spin-up orbital which exhibits Ce-$5d$ character in most cases, referring to the detailed descriptions by Canning *et al.* [35] and Jia *et al.* [36,37]. With the same basis set and pseudopotential used in ground-state and excited-state calculations, direct comparison of the calculated total energies is allowed, and the $4f \rightarrow 5d$ neutral excitation of the Ce^{3+} ion can be described through the total-energy difference within the DFT framework.

C. HSE06 calculated energies of 4*f* and 5*d* levels

Based on the GGA-PBE optimized structure of the $2 \times 2 \times 2$ $M_2B_5O_9Cl$ supercell containing 136 atoms in which a pair of M^{2+} cations was substituted by a Ce^{3+}-Na^+ pair, hybrid HSE06 calculations were adopted to obtain the position of $4f$ and $5d$ levels of Ce^{3+} in the band gap by treating the Ce-Na pair-doped supercell as a "primitive cell" of a hypothetical crystal. When the primitive cell is neutral, the calculated valence-band (VB) edge is composed of $4f$ orbitals of Ce^{3+}, while if the primitive cell is monopositive charged, the $4f$ orbitals of Ce^{3+} are unoccupied and the $5d$ orbitals of Ce^{3+} appear as several conduction bands (CBs). Each calculated band contains a single GKS eigenvalue when only one k-point Γ was adopted in the two separate HSE06 calculations on the hypothetic crystals, so the $4f$ band will be referred to as the highest occupied molecular orbital of the neutral cell, and the

5*d* band will be referred to as the lowest unoccupied molecular orbital of the monopositive charged cell analogous to the cases in molecules. It is noted that the atomic coordinates of the neutral cell were used for the monopositive charged cell so as to simulate the optical excitation process by following the Frank-Condon principle. The reduced cutoff energy was set to 400 eV and only one *k*-point Γ was adopted as a compromise between computational cost and accuracy.

We note that in our simulations the ratio of numbers of Ce to the site of Ca/Sr is actually about 6%, which is six times larger than that of the $M_{2(1-x-y)}\mathrm{Ce}(2)_x\mathrm{Na}_{2y}\mathrm{B}_5\mathrm{O}_9\mathrm{Cl}$ ($x = y = 0.01$) samples in experiments. Fortunately, it has been well known in experiments that no significant influence of the Ce^{3+} concentration was found on the emission and excitation energy spectra [59–62], apart from energy transfer and concentration quenching, which are irrelevant to our study of the energy structure of isolated dopants. Furthermore, systematic investigations on the $4f^N \rightarrow 4f^{N-1}5d$ transitions of lanthanide ions in crystals [76,77] indicate that the energy levels of doped Ce^{3+} and other lanthanide ions can be simply modeled empirically as isolated ions with ligand effects, i.e., crystal-field interactions from the host. With regard to the slight difference in ligand effects between the two cases of the Ce^{3+} centers with and without local charge compensator Na^+, the experimental results show that the excitation and emission spectra are dominated by only a single set of Ce^{3+} centers, so we only model the set of dominant centers with the $2 \times 2 \times 2$ supercell containing 136 atoms in which a pair of the nearest *M* cations is substituted by a Ce-Na pair.

D. Alternative approaches to calculate the 4*f*-valence-band-maximum energy difference

The vertical 4*f* charge transition level $\mu(+1/0)$, which is defined as the Fermi level at which the formation energies of the neutral and the monopositive charged $M_2\mathrm{B}_5\mathrm{O}_9\mathrm{Cl}$: Ce, Na supercells are equal [6], is an alternative approach to calculate the 4*f*-valence-band-maximum (VBM) energy difference. The monopositive charged supercell is created when an electron of the neutral supercell is removed. The VBM-referred $\mu(+1/0)$ is calculated by utilizing the expression [6]

$$\mu(+1/0) = E_{\mathrm{tot}}(0) - [E_{\mathrm{tot}}(+1) + E_{\mathrm{corr}} + \varepsilon_{\mathrm{VBM}}], \quad (1)$$

where $E_{\mathrm{tot}}(0)$ and $E_{\mathrm{tot}}(+1)$, respectively, stand for the total energy of the neutral and the monopositive charged supercell, and the atomic coordinate of the monopositive charged supercell was constrained to be the same as that of the neutral supercell. $\varepsilon_{\mathrm{VBM}}$ is the KS eigenvalue of the VBM of the monopositive charged supercell which has been aligned with that of the perfect $M_2\mathrm{B}_5\mathrm{O}_9\mathrm{Cl}$ crystal by the macroscopic averaging approach [6,78–80]. Charged supercells were calculated by assuming a jellium charge of opposite sign and the total energy was corrected by E_{corr} to account for electrostatic interactions between supercells, i.e., [81,82]

$$E_{\mathrm{corr}} = (1 + f)\frac{q^2\alpha_{\mathrm{M}}}{2\varepsilon L}. \quad (2)$$

Here the meanings and values adopted in our calculations are the following: $1 + f \approx 2/3$, the net charge $q = +1$ for the monopositive charged supercell in which an electron is removed, the dielectric constant $\varepsilon \approx 14$ [83], the linear supercell dimension $L = \Omega^{1/3} \approx 12$ Å (supercell volume Ω), and the Madelung-like constant $\alpha_M = 2.837$ for a cubic supercell [84]. Hence, E_{corr} is estimated to be about 0.08 eV for the monopositive charged supercell.

The DFT+*U* method of applying an orbital dependent potential that adds an extra Coulomb interaction *U* for the semicore states has been widely used to better treat the 4*f* levels of Ce and Eu [35–40]. The net effect of the added on-site Coulomb interaction is to shift the fully occupied narrow *f* bands downward by about *U*/2 in energy [41–43]. Although *U* can be determined in a self-consistent and basis-set independent way [46,47], the calculations can be cumbersome and the results are not necessarily better than those with an empirical *U* value. Systematic calculations on both scintillating and nonscintillating Ce-doped compounds by Canning *et al.* [35] indicate that an effective $U_{\mathrm{eff}} = 2.5$ eV is an appropriate approximation for the GGA(PBE)+*U* calculation of the 4*f*-VBM energy gap to match the experimental data. Hence, in our paper we adopt $U_{\mathrm{eff}}/2 = 1.25$ eV to obtain an alternative estimation of 4*f*-VBM energies and compare them with those of the HSE06 results.

E. Quantum chemical calculations by utilizing cluster models

Quantum chemical calculations for the $4f \rightarrow 5d$ transition energies by utilizing a wave-function-based embedded cluster approach [7–20] were also carried out to compare with the results obtained from the HSE06 calculation scheme outlined in Sec. II C. The Ce-centered embedded clusters $(\mathrm{Ce}_{M1}\mathrm{O}_6\mathrm{Cl}_2\mathrm{B}_3)^{2-}$ and $(\mathrm{Ce}_{M2}\mathrm{O}_6\mathrm{Cl}_2\mathrm{B}_3)^{2-}$ for two Ce sites were constructed on which the wave-function-based *ab initio* calculations were performed. The embedded cluster which comprises the central Ce^{3+} ion and its surrounding ions (including a compensating ion Na^+) within a sphere of radius 10.0 Å was modeled using the AIMP embedding potentials to account for the short-range electrostatic, exchange, and Pauli interactions of the clusters with their environments. The atomic coordinates of the ions within a sphere of radius 5.0 Å surrounding the centered Ce were simulated by utilizing the DFT-optimized structures in which a pair of M^{2+} ($M =$ Ca, Sr) cations was substituted by a Ce^{3+}-Na^+ pair. The ions beyond the embedded cluster and within the sphere of radius 30.0 Å were simulated by point charges located at $M_2\mathrm{B}_5\mathrm{O}_9\mathrm{Cl}$ lattice sites, which were generated by utilizing Gelle and Lepetit's method [85].

For these embedded clusters, state-average complete active space self-consistent field (SA-CASSCF) calculations [86] were performed with the scalar relativistic many-electron Hamiltonian, which takes into account the bonding, static, and dynamic correlation effects. These wave-function-based calculations were performed by utilizing the program MOLCAS [87]. In the SA-CASSCF calculations, a [4*f*, 5*d*, 6*s*] complete active space was adopted. The CASSCF wave functions come from interactions of all configurations in which the single unpaired electron occupies one of the 13 molecular orbitals of main characters Ce^{3+} 4*f*, 5*d*, and 6*s*. The molecular orbitals are optimized by minimizing the average energy of the 13 states [18]. In these calculations, a relativistic effective core

TABLE I. Experimental and DFT-optimized lattice parameters of pure $M_2B_5O_9Cl$ (M = Ca, Sr).

Formula	Space group	Method	a (Å)	b (Å)	c (Å)	α, β, γ (deg)
$Ca_2B_5O_9Cl$	P*nn*2	Measured[a]	11.26	11.13	6.30	90, 90,90
		Calculated	11.42	11.26	6.35	90, 90,90
$Sr_2B_5O_9Cl$	P*nn*2	Measured[b]	11.32	11.38	6.49	90, 90,90
		Calculated	11.59	11.52	6.55	90, 90,90

[a] Measured lattice parameters from Ref. [59].

[b] Measured lattice parameters from Ref. [60].

potential ([Kr] core) with a $(14s10p10d8f3g)/[6s5p6d4f1g]$ Gaussian valence basis set [88] was used for Ce, a [He] core effective core potential with a $(5s6p1d)/[2s4p1d]$ valence basis set [89] was employed for O, a [Ne] core effective potential with a $(7s7p1d)/(2s4p1d)$ valence basis set [89] was adopted for Cl, and a [He] core effective potential with a $(5s5p1d)/(2s3p1d)$ valence basis set [89] was adopted for B.

III. RESULTS AND DISCUSSIONS

A. Geometric optimizations and band-structure calculations

$M_2B_5O_9Cl$ (M = Ca, Sr) belongs to the orthorhombic system with the *Pnn*2 space group [90]. The crystal structure consists of a three-dimensional $(B_5O_9)_\infty$ network in which B_5O_{12} groups of three BO_4 tetrahedra and two BO_3 triangles are linked together. M ions occupy two slightly different crystallographic sites of 4c Wyckoff positions in $M_2B_5O_9Cl$, and are surrounded by six nearest oxygen ions and two chlorine ions with another oxygen ion located at about 3.4 Å away. For the case of $Ca_2B_5O_9Cl$, the Ca at (0.2523, 0.0475, 0) is referred to as the Ca(1) site, and the Ca at (0.0255, 0.2403, 0.6624) is referred to as the Ca(2) site [91]. The same convention is used for Sr(1) and Sr(2), though the coordinates differ slightly. As shown in Table I, the DFT-optimized lattice parameters of pure $M_2B_5O_9Cl$ (M = Ca, Sr) are slightly larger than the experimental ones [59,60] by 0.8–1.9%. The discrepancies can be traced to the inherent shortcomings of the PBE functional. Figures 1(a) and 1(b) show the relaxed structures of the unit cell of $M_2B_5O_9Cl$ (M = Ca, Sr), which contains four primitive cells. As Fig. 1(c) shows, the two quite different Ca-Cl bond lengths are 2.805 and 3.187 Å at the Ca(1) site, while the two close Ca-Cl bond lengths are 2.901 and 2.989 Å at the Ca(2) site. The two Sr sites are shown in Fig. 1(d), where the two Sr-Cl bond lengths of 2.952 and 3.121 Å are quite different at the Sr(1) site, while both of them are 3.033 Å at the Sr(2) site.

The band structures of $Ca_2B_5O_9Cl$ and $Sr_2B_5O_9Cl$ calculated with the HSE06 functional are plotted in Fig. 2. The calculated band gaps are 6.96 and 6.87 eV by utilizing the HSE06 functional, which are larger than those of 5.28 and 5.23 eV by utilizing the PBE functional. For comparison, the calculated host band gaps based on FP-LAPW method are 7.48 and 8.06 eV by utilizing the mBJ exchange potential. In experiments, the fundamental absorption edge energy of $Ca_2B_5O_9Cl$ is about 7.1 eV and the excitation spectrum of the Ce^{3+} emission shows a band with a maximum at 7.7 eV [61], so the actual gap between the VBM and conduction-band minimum (CBM) of $Ca_2B_5O_9Cl$ should be slightly larger than 7.1 eV but no more than 7.7 eV. The actual gap of $Sr_2B_5O_9Cl$ is close to that of $Ca_2B_5O_9Cl$ [92]. The above results show that the host band gaps seem to be slightly undervalued in the HSE06 calculations, while they are in much better agreement with experimental data than those derived from PBE calculations. This is in accord with previous findings that hybrid DFT yields realistic GKS gaps for typical semiconductors but tends to underestimate the band gap for wide-band-gap materials [6]. The band gaps obtained with the above methods are all calculated to be direct at Γ. From an analysis of the orbital-projected densities of states (DOSs) of $M_2B_5O_9Cl$, the dominant components of the VB are O-p characteristic, while the bottom of the CB is composed mostly of orbitals of M cations, with the orbitals of B at higher energies. Our calculated electronic structures of $M_2B_5O_9Cl$ are in qualitative agreement with previous PBE calculated results [93].

There are two M sites in $M_2B_5O_9Cl$. We refer to the Ce(1)-Na(2) site as the case of one M(1) ion being replaced by a Ce ion together with its nearest M(2) ion being replaced by a Na for charge balance, and Ce(2)-Na(1) as the case of the other way around. The structures of Ce-Na-doped supercells are optimized with GGA-PBE calculations. Calculations with both the single k-point Γ set and the 2 × 2 × 2 k-point set have been performed on the Ce(1)-Na(2) site in $Ca_2B_5O_9Cl$. The results show that the lattice parameters differ by no more than 0.04% and the Ce-O bond lengths differ by no more than 0.004 Å. Furthermore, the KS eigenvalues from the two calculations performed on the same supercell show that the shifts of the VBM and CBM are both less than 0.04 eV, and the broadenings of the Ce-4f band and the lowest Ce-5d band when Ce-4f is unoccupied are about 0.001 and 0.014 eV, respectively. Hence, the results presented hereafter are all obtained for the case of a single k-point Γ set. The optimized local structures of the two Ce-Na sites in $Ca_2B_5O_9Cl$ are schematically plotted in Figs. 1(e) and 1(f), and the bond lengths of Ce-O, Ce-Cl, and Ce-Na in $Ca_2B_5O_9Cl$ and $Sr_2B_5O_9Cl$ are listed in Table II. The GGA-PBE calculated total energy of the $Ca_2B_5O_9Cl$ supercell containing a Ce(2)-Na(1) pair is 0.23 eV higher than that containing a Ce(1)-Na(2) pair, while the total energy of the $Sr_2B_5O_9Cl$ supercell containing a Ce(2)-Na(1) pair is 0.1 eV lower than that containing a Ce(1)-Na(2) pair. From our DFT calculated total energy of the doped supercell, it is revealed that in $Ca_2B_5O_9Cl$ the Ce-Na pairs prefer to occupy the Ce(1)-Na(2) site over the Ce(2)-Na(1) site, and in $Sr_2B_5O_9Cl$ the Ce-Na pairs have slightly more tendency to occupy the Ce(2)-Na(1) site. The relative stability of these sites

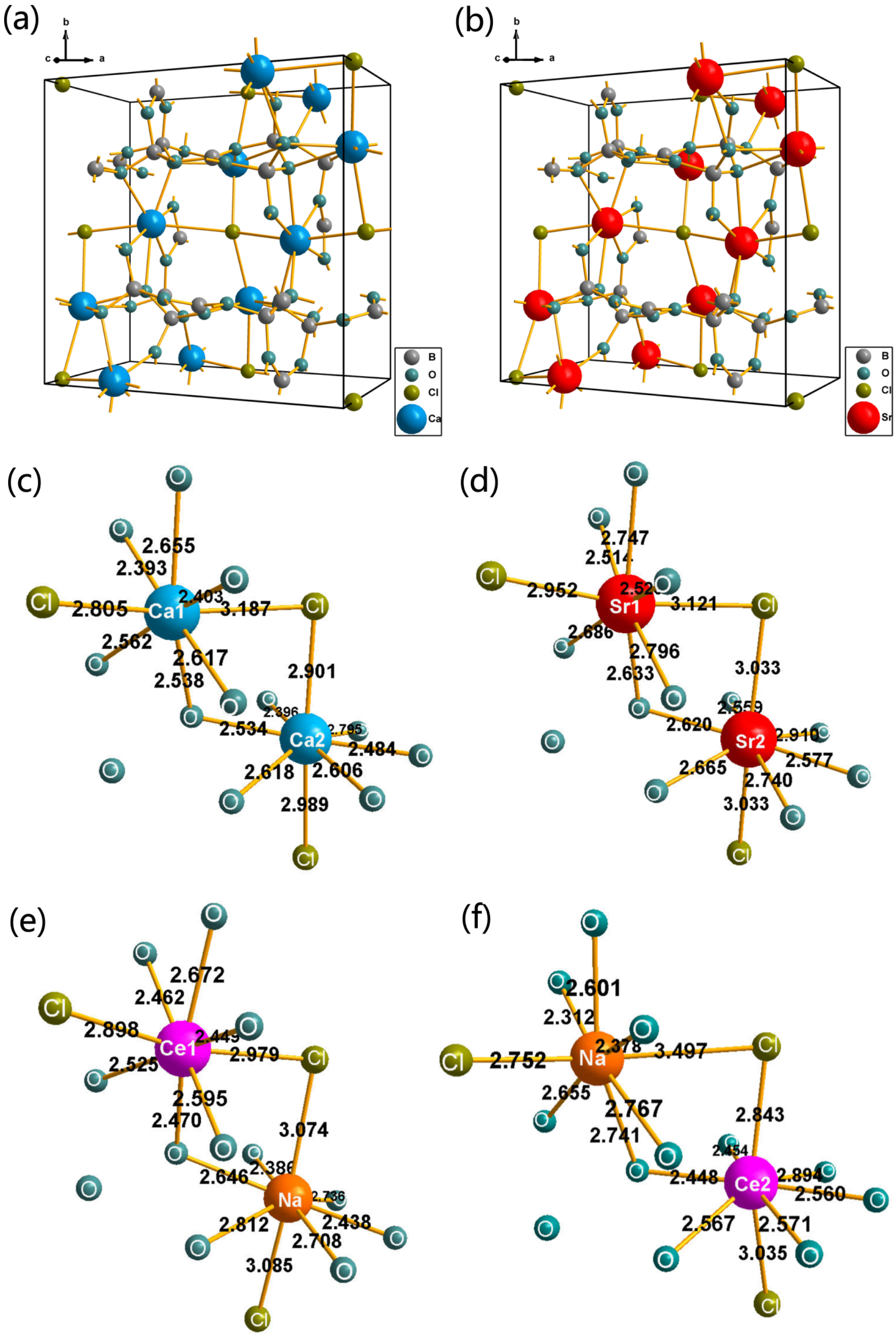

FIG. 1. (a, b) The unit-cell structures of $Ca_2B_5O_9Cl$ (a) and $Sr_2B_5O_9Cl$ (b) after DFT calculations of atomic relaxation. (c, d) The local structures of the two Ca sites in $Ca_2B_5O_9Cl$ (c) and the two Sr sites in $Sr_2B_5O_9Cl$ (d). (e, f) The local structures of the Ce(1)-Na(2) site (e) and the Ce(2)-Na(1) site (f) in $Ca_2B_5O_9Cl$. It is noted that the unit cell in panels (a) and (b) contains four primitive cells.

can be qualitatively understood by the valences for Ce and Na derived from their corresponding coordination structures using the bond-valence sum (BVS) method [94], which refers to their corresponding formal valences (+3 for Ce and +1 for Na). The BVS values for Ce and Na are listed in the bottom two rows of Table II. In the Ce-Na pair-doped $Ca_2B_5O_9Cl$, the BVS value of Ce at the Ce(1)-Na(2) site (+2.987) is much closer to the formal value +3 than that at the Ce(2)-Na(1) site (+2.857), while the BVS values of Na at the two sites (+0.913 and +1.092) both have a deviation of about 0.09 from the formal value +1; in Ce-Na pair-doped $Sr_2B_5O_9Cl$, though, the Ce at the two sites have similar BVS values (+2.762 and +2.763), while the BVS value of Na at the Ce(2)-Na(1) site (+0.993) is much closer to the formal value +1 than that at

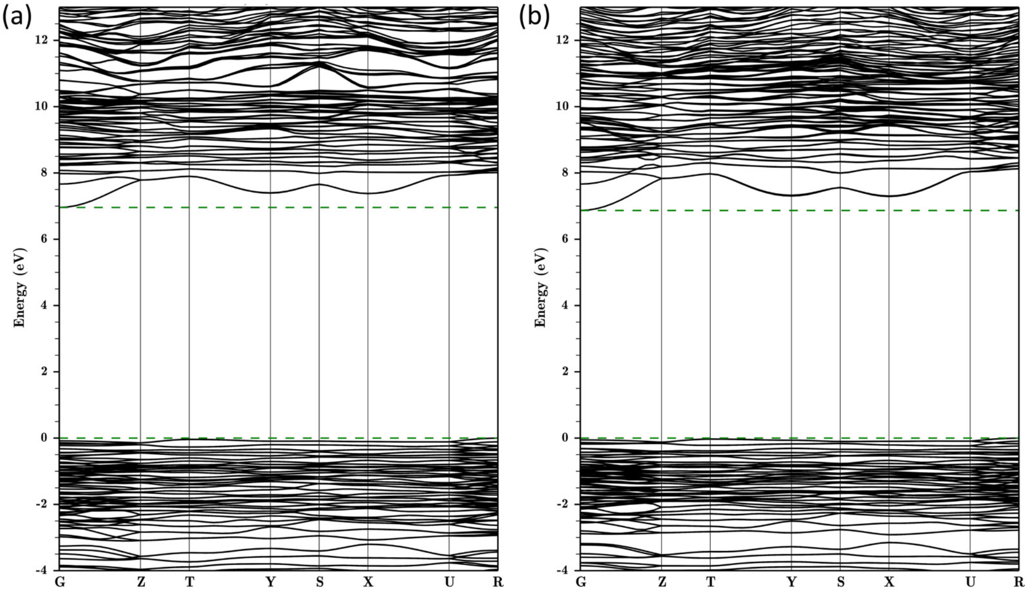

FIG. 2. The band structures of $Ca_2B_5O_9Cl$ (a) and $Sr_2B_5O_9Cl$ (b) by utilizing the HSE06 functional.

the Ce(1)-Na(2) site (+0.831). In short, the BVS values show greater stability for the Ce-Na pair at the Ce(1)-Na(2) site in $Ca_2B_5O_9Cl$, while they show greater stability for the Ce-Na pair at the Ce(2)-Na(1) site in $Sr_2B_5O_9Cl$; this is consistent with the results derived from our DFT calculated total energies of the-doped supercells. As the dominant contribution to the BVS of a cation comes from its coordination anions, the average bond length of Ce-O_m (m = 1–6), which is denoted as $\mathbf{A_6}$ in Table II, can be a rough indication of the favorability of one Ce site over the other. The ground-state $\mathbf{A_6}$ at the

TABLE II. The Ce-O, Ce-Cl, and Ce-Na bond lengths (in Å) of optimized geometric configurations. The valence for Ce and Na derived from their corresponding coordination structures using the bond-valence sum (BVS) method [94].

Host	$Ca_2B_5O_9Cl$				$Sr_2B_5O_9Cl$			
site	Ce(1)-Na(2)		Ce(2)-Na(1)		Ce(1)-Na(2)		Ce(2)-Na(1)	
state	*G*[a]	*E*[a]	*G*	*E*	*G*	*E*	*G*	*E*
Ce-O_1[b]	2.449	2.400	2.448	2.425	2.488	2.444	2.450	2.464
Ce-O_2	2.462	2.440	2.454	2.459	2.501	2.468	2.528	2.472
Ce-O_3	2.470	2.454	2.560	2.519	2.525	2.509	2.543	2.508
Ce-O_4	2.525	2.500	2.567	2.558	2.572	2.568	2.629	2.645
Ce-O_5	2.595	2.607	2.571	2.577	2.650	2.668	2.653	2.668
Ce-O_6	2.672	2.672	2.894	2.863	2.810	2.774	2.664	2.676
A_6[c]	2.529	2.512	2.582	2.567	2.591	2.572	2.578	2.572
ΔO[d]		0.65%		–0.59%		–0.74%		–0.22%
Ce-O_7[b]	3.350	3.425	2.955	3.015	3.060	3.268	3.088	3.084
(Ce-O_7)/A_6	132%	136%	114%	117%	118%	127%	120%	120%
Ce-Cl_1[b]	2.897	2.861	2.842	2.834	2.886	2.874	2.859	2.882
Ce-Cl_2	2.979	2.956	3.037	2.966	2.929	2.887	2.981	2.905
ΔCl[d]		–1.00%		–1.34%		–0.93%		–0.91%
Ce-Na[e]	4.146	4.135	4.128	4.130	4.211	4.200	4.193	4.165
V_{Ce}[f]	+2.987		+2.857		+2.762		+2.763	
V_{Na}[g]	+0.913		+1.092		+0.831		+0.993	

[a] *G* and *E*, respectively, stand for the equilibrium geometric configuration of the ground state and of the excited state.

[b] Ce-O_m (m = 1–7) and Ce-Cl_n (n = 1, 2), respectively, stand for the calculated bond length of Ce-O_m and of Ce-Cl_n.

[c] Averaged bond length of Ce-O_m (m = 1–6).

[d] ΔO and ΔCl, respectively, stand for the change of the averaged bond length of Ce-O_m (m = 1–6) and of Ce-Cl_n (n = 1, 2) at the excited $(Ce^{3+})^*$ state relative to that at the ground Ce^{3+} state.

[e] The calculated bond length of Ce-Na in equilibrium geometric configuration.

[f] Valence of Ce by BVS method.

[g] Valence of Na by BVS method.

Ce(1)-Na(2) site (2.529 Å) is shorter than that at the Ce(2)-Na(1) site (2.582 Å) in $Ca_2B_5O_9Cl$, while it is slightly longer at the Ce(1)-Na(2) site (2.591 Å) than at the Ce(2)-Na(1) site (2.578 Å) in $Sr_2B_5O_9Cl$. To sum up, the DFT-optimized local structure of Ce supports the validity of the total-energy calculated site occupation preference of the Ce(1) site [with Na compensates at the nearest Na(2) site] in $Ca_2B_5O_9Cl$ and the preference of the Ce(2) site [with Na compensates at the nearest Na(1) site] in $Sr_2B_5O_9Cl$.

We have also carried out calculations on monopositive charged supercells, which will be needed later on in discussing the thermal quenching luminescence properties. The relaxation energy of the monopositive charged supercell when the atomic coordinates change from the equilibrium of the neutral supercell to those of the monopositive charged supercell in $Ca_2B_5O_9Cl$ is obtained to be 0.32 and 0.48 eV for the Ce(1)-Na(2) site and Ce(2)-Na(1) site, respectively. For the two sites in $Sr_2B_5O_9Cl$, the corresponding relaxation energies are 0.31 and 0.29 eV.

B. Constrained occupancy approach for excited-state geometry configuration

The constrained occupancy approach was selected to determine the equilibrium configuration of the excited state $(Ce^{3+})^*$ by evacuating the seven spin-up predominantly Ce-4f orbitals and filling the next spin-up predominantly Ce-5d orbital. As listed in Table II, the averaged bond length of Ce-O_m ($m = 1$–6) and Ce-Cl_n ($n = 1$, 2) at the excited $(Ce^{3+})^*$ state decreased slightly relative to those at the ground-state Ce^{3+}. According to the Frank-Condon principle, the measured absorption and emission peaks of Ce^{3+} can be described as vertical transitions. With the atomic coordinates of both the ground state and the excited state obtained, the absorption or emission energy can be calculated as the total-energy difference between the two states. Although DFT, as a ground-state theory, is unable to produce accurate optical absorption and emission energies, the constrained GGA-PBE approach calculated transition energies between the lowest excited state and the ground state is still useful as a guidance in phosphor research. As listed in Table III, the absorption energies are within 0.5 eV lower than the experimental data of Ce-doped $Ca_2B_5O_9Cl$ and $Sr_2B_5O_9Cl$ samples in which the shortest peaking wavelengths are 314 nm (3.95 eV) and 308 nm (4.03 eV), respectively [61]. As the 4f orbit is closer to the nuclei than the 5d orbit, when the 4f orbit is empty, the effective nuclei charge increases, leading to a downward shift of the energy of the 5d level [35].

The relaxation energy for the lowest 5d excited state when the atomic coordinates change from the equilibrium of the ground state to that of the 5d state in $Ca_2B_5O_9Cl$ is obtained to be 0.10 and 0.05 eV for the Ce(1)-Na(2) site and Ce(2)-Na(1) site, respectively. For the two sites in $Sr_2B_5O_9Cl$, the corresponding relaxation energies are 0.09 and 0.08 eV. As listed in Table III, the Stokes shift, calculated as the difference between absorption and emission photon energies, is obtained to be 0.22 and 0.11 eV for the Ce(1)-Na(2) site and Ce(2)-Na(1) site in $Ca_2B_5O_9Cl$, and the corresponding values are 0.19 and 0.16 eV in $Sr_2B_5O_9Cl$. It is noted that Ce prefers to occupy the Ce(1)-Na(2) site in $Ca_2B_5O_9Cl$, while Ce can occupy both of the two sites in $Sr_2B_5O_9Cl$ with slightly different absorption and emission energies, as indicated by the site occupation preference calculations in Sec. III A. As a result, the calculated small Stokes shifts, which can be traced to the small variation of the local structure of Ce at the excited $(Ce^{3+})^*$ state in comparison with that at the ground Ce^{3+} state as indicated by the bond lengths listed in Table II, are in good agreement with the measured Stokes shifts of 0.22 eV in $Ca_2B_5O_9Cl$ and 0.21 eV in $Sr_2B_5O_9Cl$ as listed in Table III.

TABLE III. PBE density functional calculated absorption, emission, and Stokes shift (in eV). The experimental data are listed for comparison.

		Abs.			ΔS	
M	Site	Calc.[a]	Expt.[b]	Em. calc.[a]	Calc.[a]	Expt.[b]
Ca	Ce(1)-Na(2)	3.47	3.95	3.25	0.22	0.22
	Ce(2)-Na(1)	3.39		3.28	0.11	
Sr	Ce(1)-Na(2)	3.66	4.03	3.47	0.19	0.21
	Ce(2)-Na(1)	3.70		3.55	0.16	

[a] PBE density functional calculated data.

[b] Experimental data in Ref. [61].

C. HSE06 calculated energies of 4f and 5d levels relative to band edges

Based on the GGA-PBE optimized structure of the 2 × 2 × 2 $M_2B_5O_9Cl$ supercell containing 136 atoms in which a pair of M^{2+} cations is substituted by a Ce^{3+}-Na^+ pair, two separate HSE06 calculations on a neutral and on a monopositive charged supercell were adopted to obtain the position of 4f and 5d levels of Ce^{3+} in the band gap. Figure 3 plots the total and orbital-projected DOSs by utilizing only one k-point Γ to sample the Brillouin zone. Figure 3 clearly indicates that the calculated valence-band edge is composed of 4f orbitals of Ce^{3+} when the cell is neutral, but when the cell is monopositive charged the calculated several lower conduction bands are of Ce-5d character exhibiting crystal-field splitting. It is noteworthy that the atomic coordinate of the monopositive charged cell that we adopted was constrained to be the same as that of the neutral cell to simulate the vertical 4f → 5d transitions. After the two separate HSE06 calculations, the 4f band was compared with the predominantly VBM orbital of the host to obtain the 4f-VBM energy difference, which is defined as the energy released by a hole at the VBM through vertical transition (without geometric relaxation) to the Ce^{3+} impurity in the ground state; the lowest 5d band was compared with the predominantly CBM orbital of the host to obtain the CBM-5d energy difference, which is defined as the energy required by the electron of the Ce^{3+} impurity at a lowest excited state of 5d character through vertical ionization to the CBM. After the 4f-VBM and CBM-5d energy differences are obtained, the 4f → 5d energies can be obtained by subtracting the 4f-VBM and CBM-5d energies from the corresponding host band gaps (6.96 and 6.87 eV for $Ca_2B_5O_9Cl$ and $Sr_2B_5O_9Cl$, respectively, as shown in Fig. 2). As shown in Table IV and Fig. 4, the calculated 4f → 5d excitation energies can be

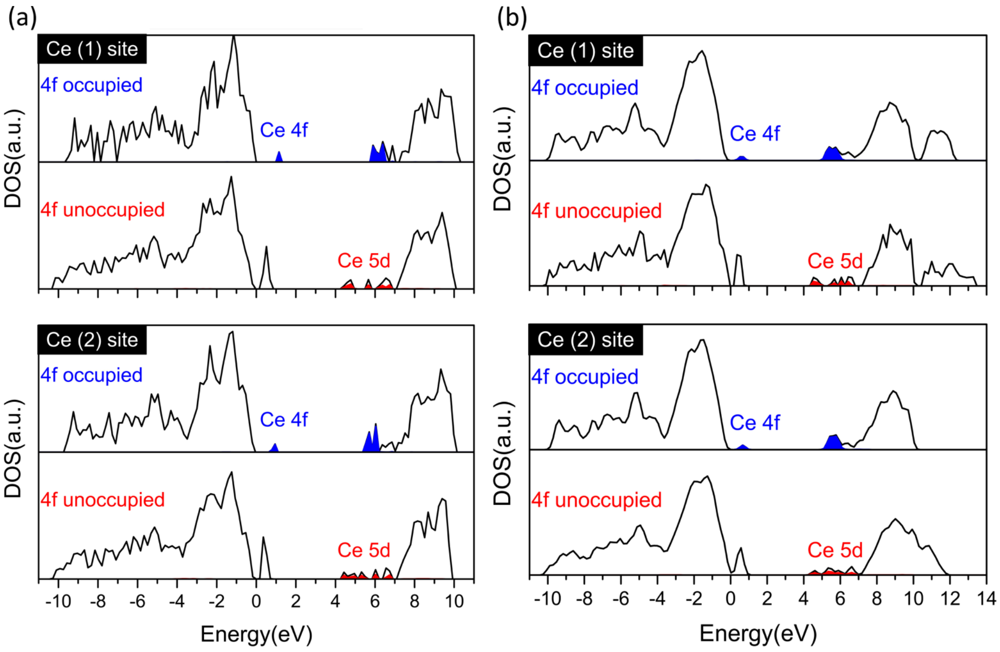

FIG. 3. Total and orbital-projected DOSs for the Ce-Na pair-doped 2 × 2 × 2 $Ca_2B_5O_9Cl$ (a) and $Sr_2B_5O_9Cl$ (b) supercell. The calculations are carried out by using DFT with the HSE06 hybrid functional and only one k-point Γ to sample the Brillouin zone. The VBM is set at zero energy.

compared with the experimental data [61,62] from the excitation spectra of $M_{2(1-x-y)}\mathrm{Ce}(2)_x\mathrm{Na}_{2y}\mathrm{B}_5\mathrm{O}_9\mathrm{Cl}$ ($x = y = 0.01$). It is noted that the calculated $4f \rightarrow 5d$ excitation energies are undervalued. This can mainly be attributed to the slight underestimation of the host band gaps. Another correction to the $4f$-$5d$ energy difference, which is estimated to be a blueshift of about $2\zeta_{4f} = 0.15\,\mathrm{eV}$, is the impact of spin-orbit interaction by adopting $\zeta_{4f} \approx 615\,\mathrm{cm}^{-1}$ [76]. Hence, the calculated lowest $5d$ level was aligned with the measured one, as shown in Fig. 4, for a more intuitive comparison with the experimental measured $5d$ crystal-field levels by considering that the lowest $5d$ level is generally much better defined than the high-lying ones both in calculations and in experimental measurements. It is indicated that the calculated $5d$ splitting of Ce at the Ce(1) site [with Na compensates at the nearest Na(2) site] in $Ca_2B_5O_9Cl$ has more consistency with the measured data than the results of Ce at the Ce(2) site [with Na compensates at the nearest Na(1) site], supporting the validity of the total-energy calculation, which indicates occupation preference of Ce at the Ce(1) site in $Ca_2B_5O_9Cl$. Referring to the excitation spectrum of $\mathrm{Sr}_{2(1\text{-}x)}\mathrm{Ce}_x\mathrm{Na}_x\mathrm{B}_5\mathrm{O}_9\mathrm{Cl}$ ($x = 0.01$) [61,62], which resolves altogether six peaks being

TABLE IV. $4f$-VBM, CBM-$5d$, and $4f \rightarrow 5d$ energies (in eV) of $M_2B_5O_9Cl$: Ce, Na (M = Ca, Sr).

				$4f \rightarrow 5d_i$, i = 1–5[a]					
M	Site	Method	$4f$-VBM	1	2	3	4	5	CBM-$5d_1$
Ca	Ce(1)-Na(2)	HSE06	1.38	3.65	3.93	4.80	5.43	5.80	1.93
	Ce(2)-Na(1)		1.22	3.78	4.16	4.67	5.33	5.96	1.96
	Ce	Expt.[b]		3.95	4.29	5.23	5.77	6.20	
	Ce(1)-Na(2)	AIMP		3.88	4.28	5.68	5.74	6.02	
	Ce(2)-Na(1)			4.05	4.41	5.08	5.95	6.19	
Sr	Ce(1)-Na(2)	HSE06	1.18	3.84	4.13	4.94	5.41	5.74	1.85
	Ce(2)-Na(1)		1.22	3.85	4.57	4.75	5.19	5.86	1.80
	Ce	Expt.[b]		4.03	4.44 4.59	5.30	5.66	6.14	
	Ce(1)-Na(2)	AIMP		4.00	4.33	5.47	5.77	6.03	
	Ce(2)-Na(1)			4.06	4.58	5.06	5.66	6.05	

[a] $4f \rightarrow 5d_1$ is obtained as E_g(host)–($4f$-VBM)–(CBM-$5d_1$), and $4f \rightarrow 5d_i$ (i = 2–5) are obtained by identifying approximately the differences in GKS energy among $5d_i$ as $5d$ crystal-field splitting. Calculated $E_g(\mathrm{Ca_2B_5O_9Cl}) = 6.96\,\mathrm{eV}$ and $E_g(\mathrm{Sr_2B_5O_9Cl}) = 6.87\,\mathrm{eV}$ are used.

[b] Experimental data from the excitation spectra of $M_2B_5O_9Cl$: Ce, Na (M = Ca, Sr) by monitoring the $5d \rightarrow 4f$ emission of Ce^{3+} in Refs. [61,62].

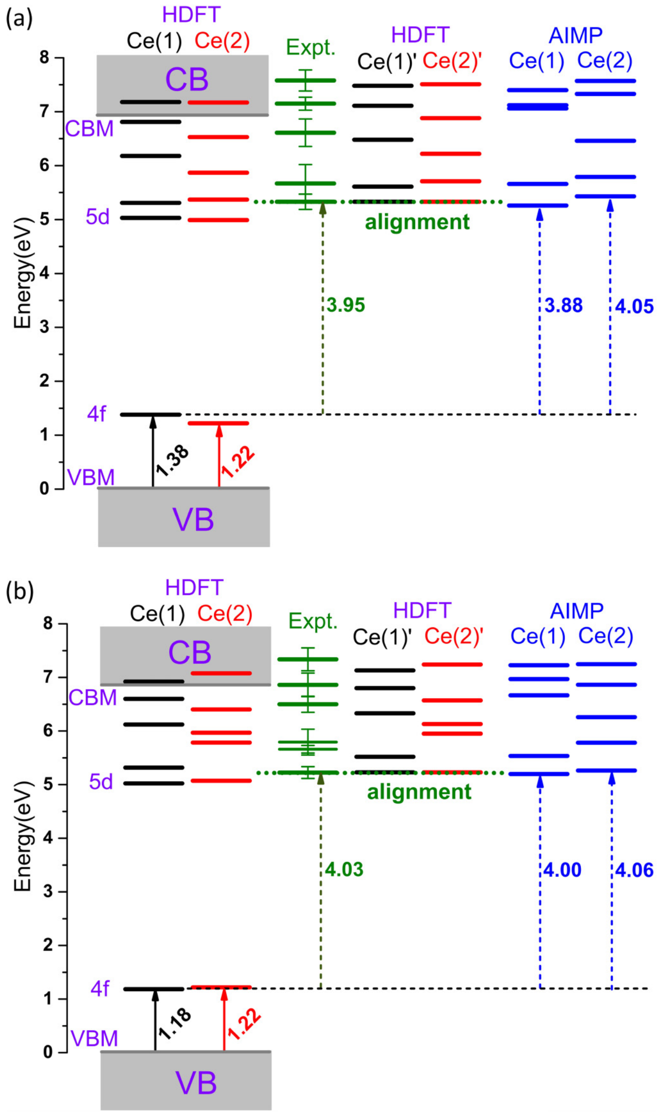

FIG. 4. Comparison of calculated Ce^{3+} levels with experimental data. In $Ca_2B_5O_9Cl$ (a) and $Sr_2B_5O_9Cl$ (b), HDFT Ce(1) and Ce(2) are the HSE06 energy levels of the two Ce sites with respect to host band edges. The experimental data of $5d$ levels relative to $4f$ (marked as Expt.) are plotted in column 3, and the error bar shows the full width at half maximum of the experimental data. After aligning the HSE06 calculated lowest $5d$ level with the measured one, the HSE06 calculated $5d$ levels for the Ce (1) site and Ce (2) site are plotted in column 4 and column 5 and denoted as HDFT Ce (1)' and HDFT Ce (2)'. The AIMP calculated $5d$ levels are plotted as AIMP Ce (1) and AIMP Ce (2) for the two sites.

identified as $4f \rightarrow 5d$ transitions, as schematically shown in Fig. 4, the HSE06 calculated $5d$ splitting of Ce in $Sr_2B_5O_9Cl$ supports the existence of both of the two Ce-Na sites. Furthermore, the calculated $5d_1$–$5d_4$ levels in both $Ca_2B_5O_9Cl$ and $Sr_2B_5O_9Cl$ are unambiguously below the host CBM, while the fifth $5d$ mixes with the host CBM and tends to spread out slightly, which agrees well with the corresponding excitation spectra where all of the five Ce^{3+} $4f \rightarrow 5d$ bands are clearly observed and the lower four excitation peaks are particularly strong [61,62].

TABLE V. PBE density functional calculated $4f$-VBM with VBM-referred $\mu(+1/0)$ and with DFT+U treatment ($U_{\mathrm{eff}} = 2.5$ eV).

M	Site	$\mu(+1/0)$	PBE+U
Ca	Ce(1)-Na(2)	0.87	1.63
	Ce(2)-Na(1)	0.92	1.34
Sr	Ce(1)-Na(2)	0.62	1.04
	Ce(2)-Na(1)	0.64	1.05

Here we consider the thermal quenching of the photoluminescence of Ce^{3+} in $M_2B_5O_9Cl$ due to the following two processes considered in Ref. [95], with one described by the $5d$-$4f$ crossing model and the other by the Dorenbos autoionization model. In the $5d$-$4f$ crossing model, the luminescent center relaxes thermally from the excited state to the ground state via the crossover point of the energy curves of the $5d$ excited state and the $4f$ ground state. The energy barrier E_A for the crossover point can be calculated by extrapolating the configuration diagram energy curves from the energies and equilibrium positions of $4f$ and $5d$ states under harmonic approximation. E_A is roughly calculated to be even higher than 8 eV for all the four sites of Ce^{3+} in $M_2B_5O_9Cl$, showing that the contribution of such a process to thermal quenching is negligible. The Dorenbos autoionization model describes the thermal quenching by thermal ionization of the luminescent center in the excited state to the conduction band [96]. The energy difference E_I between the $5d$ excited state and ionized state at their corresponding equilibrium atomic configurations differs from the CBM-$5d_1$ energy gap obtained from the HSE06 calculation at the ground-state equilibrium atomic configuration, since there are relaxation energies between different atomic configurations for the initial and final states. With the HSE06 calculated CBM-$5d_1$ gap (as listed in the rightmost column of Table IV) and the relaxation energies for the ionized state (Sec. III A) and for the $5d$ excited state (Sec. III B), we estimate the autoionization energy E_I to be 1.71 and 1.53 eV for the Ce(1)-Na(2) site and Ce(2)-Na(1) site in $Ca_2B_5O_9Cl$, respectively. For the two sites in $Sr_2B_5O_9Cl$, the corresponding E_I values are 1.63 and 1.59 eV. These high E_I values show that the quenching due to autoionization is not severe either, hinting that very high thermal quenching temperatures are expectable for the two phosphors.

D. Miscellaneous discussions

As shown in Table IV and Fig. 4, the Ce^{3+} $4f$-VBM gaps in $Ca_2B_5O_9Cl$ obtained by HSE06 calculation are 1.38 and 1.22 eV for the Ce(1)-Na(2) site and Ce(2)-Na(1) site, respectively. The corresponding values are 1.18 and 1.22 eV in $Sr_2B_5O_9Cl$. As an alternative approach to obtain the $4f$-VBM energy difference, the vertical $4f$ charge transition level $\mu(+1/0)$ is calculated using Eq. (1). As listed in Table V, the VBM-referred $\mu(+1/0)$ in $Ca_2B_5O_9Cl$ are 0.87 and 0.92 eV for the Ce(1)-Na(2) site and Ce(2)-Na(1) site, respectively. The corresponding values are 0.62 and 0.64 eV in $Sr_2B_5O_9Cl$. The DFT+U treatment ($U_{\mathrm{eff}} = 2.5$ eV) to the $4f$-VBM KS energy difference was applied to overcome the underestimation of the localization of the $4f$ state, and the obtained $4f$-VBMs in $Ca_2B_5O_9Cl$ are 1.63 and 1.34 eV for the Ce(1)-Na(2) site and Ce(2)-Na(1) site, respectively. The corresponding values are 1.04 and 1.05 eV in $Sr_2B_5O_9Cl$. The $4f$-VBM gaps obtained with DFT+U treatment are similar to those obtained with hybrid HSE06 calculations, while the VBM-referred charge transition levels $\mu(+1/0)$ are smaller and are almost the same for Ce at the two sites in a certain host. As the standard DFT calculations with the GGA-PBE functional substantially undervalued the band gaps, the $\varepsilon_{\mathrm{VBM}}$ is usually overvalued, and this inevitably leads to an underestimation of VBM-referred $\mu(+1/0)$ as expressed in Eq. (1). The position of the $4f$ level of Ce in the host band gap is likely to vary with the local structure of Ce. From the Ce-O bond lengths in the ground-state geometric configurations as listed in Table II, the bond length ratio of the seventh Ce-O to the average of the six shortest Ce-O_m ($m = 1$–6) is calculated to be 132 and 114% for the Ce(1)-Na(2) site and Ce(2)-Na(1) site in $Ca_2B_5O_9Cl$, while the corresponding ratios are 118 and 120% in $Sr_2B_5O_9Cl$. So, the obvious difference between the $4f$-VBM energies for the two sites in $Ca_2B_5O_9Cl$, which is obtained with hybrid HSE06 calculations or with DFT+U treatment, may largely be attributed to the quite different oxygen coordinations of Ce at the two sites.

The $4f \rightarrow 5d$ transition energies calculated by utilizing the embedded cluster approach are listed in Table IV and plotted in Fig. 3. It is revealed that the obtained $5d$ crystal-field splitting shows some correlation with experimental measurements, and it is noted that the centroid energy of $5d$ calculated by utilizing the cluster model is in better agreement with experiment than that obtained with the HSE06 calculation. As mentioned in Sec. III A, the calculated band gap of $Ca_2B_5O_9Cl$ by utilizing the mBJ approach is about 0.5 eV larger than that by utilizing the HSE06 functional. Although in this paper we choose hybrid HSE06 with fixed hybrid parameters ($\alpha = 0.25$, $\mu = 0.2$) in the calculation scheme by considering the computational efficiency and the general applicability for various materials, actually, material dependent parameters α and μ could be adjusted to produce more accurate results to agree reasonably well with experiments. It has been found that there is an almost linear correlation between the optimized α parameter (by setting $\mu = 0$) and the inverse of the static dielectric constant $1/\varepsilon_\infty$ [97–99]. Moreover, Deák *et al.* [100] presented a method to determine optimal α and μ that not only produces the correct optical band gap but also ensures that the defect levels in the gap satisfy the generalized Koopmans theorem [101]. It is foreseeable that the predicted $4f$-$5d$ energy gap will be much closer to measured values by utilizing more appropriate hybrid parameters.

IV. CONCLUSION

A systematic first-principles study on not only the ground and the excited states of Ce^{3+} but also their relative positions with respect to the host band edges in Ce-doped $M_2B_5O_9Cl$ ($M =$ Ca, Sr) with Na as charge compensator has been carried out by combining the constrained occupancy approach and the hybrid HSE06 calculation in the framework of a generalized Kohn-Sham formalism. First, ground-state total-energy calculations indicate that Ce prefers occupying the Ce(1) site to the Ce(2) site by 0.23 eV in $Ca_2B_5O_9Cl$, and Ce prefers occupying the Ce(2) site to the Ce(1) site by 0.1 eV in $Sr_2B_5O_9Cl$. Second, the obtained absorption and emission energies, the Stokes shifts, and the $5d$ crystal-field splitting not only agree reasonably well with experiments but also support our calculated site occupation preference of Ce. Third, $4f$ and the four lower $5d$ bands unambiguously reside in the host band gap, and this agrees well with the corresponding experimental spectra where five Ce^{3+} $4f \rightarrow 5d$ bands are clearly observed and the lower four excitation peaks are particularly strong.

The results obtained demonstrate that by combining the constrained occupation approach and hybrid density functional calculations the absorption and emission energies of $4f$-$5d$ transitions and Stokes shifts can be obtained, and the relative positions of the $4f$ ground and $5d$ excited states (in terms of ionization) with respect to the host band edges and the crystal-field splitting of $5d$ can be well predicted. As the structural optimizations are carried out at conventional density functional levels and only two electronic structure calculations on static atomic configurations are required within the hybrid DFT framework, the moderate calculation costs in such calculations are suitable for high-throughput predictions of luminescent properties of lanthanide-doped materials.

ACKNOWLEDGMENTS

The numerical calculations in this paper have been done on the supercomputing system in the Supercomputing Center of University of Science and Technology of China. This work was financially supported by the National Key Research and Development Program of China (Grants No. 2018YFA0306600 and No. 2016YFB0701001), the National Natural Science Foundation of China (Grants No. 61635012 and No. 11574298), and University Science Research Project of Anhui Province (Grant No. KJ2017A791). We also gratefully acknowledge financial support from the Committee on Research and Development and Dean's Research Grants of the Faculty of Liberal Arts and Social Sciences of The Education University of Hong Kong.

---

[1] E. V. D. van Loef, P. Dorenbos, C. W. E. van Eijk, K. Krämer, and H. U. Güdel, Appl. Phys. Lett. **79**, 1573 (2001).
[2] M. Sato, S. W. Kim, Y. Shimomura, T. Hasegawa, K. Toda, and G. Adachi, Handb. Phys. Chem. Rare Earths **49**, 1 (2016).
[3] X. Qin, X. Liu, W. Huang, M. Bettinelli, and X. Liu, Chem. Rev. **117**, 4488 (2017).
[4] Z. Xia and A. Meijerink, Chem. Soc. Rev. **46**, 275 (2017).
[5] P. A. Rodnyi, *Physical Processes in Inorganic Scintillators* (CRC, Boca Raton, FL, 1997).
[6] C. Freysoldt, B. Grabowski, T. Hickel, J. Neugebauer, G. Kresse, A. Janotti, and C. G. Van de Walle, Rev. Mod. Phys. **86**, 253 (2014).
[7] N.W. Winter and R. M. Pitzer, J. Chem. Phys. **89**, 446 (1988).
[8] I. de P. R. Moreira and F. Illas, Phys. Rev. B **55**, 4129 (1997).

[9] F. Illas and G. Pacchioni, J. Chem. Phys. **108**, 7835 (1998).
[10] C. Sousa, G. Pacchioni, and F. Illas, Surf. Sci. **429**, 217 (1999).
[11] J. A. Mejias, V. Staemmler, and H. J. Freund, J. Phys.: Condens. Matter **11**, 7881 (1999).
[12] C. Sousa, C. de Graaf, and F. Illas, Phys. Rev. B **62**, 10013 (2000).
[13] D. Munoz, I. de P. R. Moreira, and F. Illas, Phys. Rev. B **65**, 224521 (2002).
[14] J. Carrasco, C. Sousa, F. Illas, P. V. Sushko, and A. L. Shluger, J. Chem. Phys. **125**, 074710 (2006).
[15] Z. Barandiarán and L. Seijo, J. Chem. Phys. **89**, 5739 (1988).
[16] J. L. Pascual, J. Schamps, Z. Barandiarán, and L. Seijo, Phys. Rev. B **74**, 104105 (2006).
[17] J. Gracia, L. Seijo, Z. Barandiarán, D. Curulla, H. Niemansverdriet, and W. van Gennip, J. Lumin. **128**, 1248 (2008).
[18] L. Ning, L. Lin, L. Li, C. Wu, C. Duan, Y. Zhang, and L. Seijo, J. Mater. Chem. **22**, 13723 (2012).
[19] L. Ning, X. Ji, Y. Dong, W. Jin, Y. Huang, Z. Pan, and P. A. Tanner, J. Mater. Chem. C **4**, 5214 (2016).
[20] L. Ning, X. Huang, Y. Huang, and P. A. Tanner, J. Mater. Chem. C **6**, 6637 (2018).
[21] P. Hohenberg and W. Kohn, Phys. Rev. **136**, B864 (1964).
[22] W. Kohn, Rev. Mod. Phys. **71**, S59 (1999).
[23] A. Alkauskas, M. D. McCluskey, and C. G. Van de Walle, J. Appl. Phys. **119**, 181101 (2016).
[24] V. I. Anisimov, J. Zaanen, and O. K. Andersen, Phys. Rev. B **44**, 943 (1991).
[25] R. L. Martin and F. Illas, Phys. Rev. Lett. **79**, 1539 (1997).
[26] I. de P. R. Moreira, F. Illas, and R. L. Martin, Phys. Rev. B **65**, 155102 (2002).
[27] J. K. Perry, J. Tahir-Kheli, and W. A. Goddard III, Phys. Rev. B **63**, 144510 (2001).
[28] L. Hedin, Phys. Rev. **139**, A796 (1965).
[29] F. Bruneval and X. Gonze, Phys. Rev. B **78**, 085125 (2008).
[30] J. A. Berger, L. Reining, and F. Sottile, Phys. Rev. B **82**, 041103 (2010).
[31] B. C. Shih, Y. Xue, P. Zhang, M. L. Cohen, and S. G. Louie, Phys. Rev. Lett. **105**, 146401 (2010).
[32] G. Samsonidze, M. Jain, J. Deslippe, M. L. Cohen, and S. G. Louie, Phys. Rev. Lett. **107**, 186404 (2011).
[33] J. Deslippe, G. Samsonidze, M. Jain, M. L. Cohen, and S. G. Louie, Phys. Rev. B **87**, 165124 (2013).
[34] S. Lany and A. Zunger, Phys. Rev. B **81**, 113201 (2010).
[35] A. Canning, A. Chaudhry, R. Boutchko, and N. Grønbech-Jensen, Phys. Rev. B **83**, 125115 (2011).
[36] Y. Jia, A. Miglio, S. Poncé, X. Gonze, and M. Mikami, Phys. Rev. B **93**, 155111 (2016).
[37] Y. Jia, S. Poncé, A. Miglio, M. Mikami, and X. Gonze, Adv. Opt. Mater. **5**, 1600997 (2017).
[38] A. Chaudhry, R. Boutchko, S. Chourou, G. Zhang, N. Grønbech-Jensen, and A. Canning, Phys. Rev. B **89**, 155105 (2014).
[39] M. H. Du and K. Biswas, J. Lumin, **143**, 710 (2013).
[40] M. H. Du, ECS J. Solid State Sci. Technol. **5**, R3007 (2016).
[41] V. I. Anisimov, F. Aryasetiawan, and A. I. Lichtenstein, J. Phys. Condens. Matter **9**, 767 (1997).
[42] S. L. Dudarev, G. A. Botton, S. Y. Savrasov, C. J. Humphreys, and A. P. Sutton, Phys. Rev. B **57**, 1505 (1998).
[43] E. Finazzi, C. Di Valentin, G. Pacchioni, and A. Selloni, J. Chem. Phys. **129**, 154113 (2008).
[44] W. E. Pickett, S. C. Erwin, and E. C. Ethridge, Phys. Rev. B **58**, 1201 (1998).
[45] G. K. H. Madsen and P. Novák, Europhys. Lett. **69**, 777 (2005).
[46] M. Cococcioni and S. de Gironcoli, Phys. Rev. B **71**, 035105 (2005).
[47] A. Janotti, D. Segev, and C. G. Van de Walle, Phys. Rev. B **74**, 045202 (2006).
[48] I. Timrov, N. Marzari, and M. Cococcioni, Phys. Rev. B **98**, 085127 (2018).
[49] G. Pacchioni, F. Frigoli, D. Ricci, and J. A. Weil, Phys. Rev. B **63**, 054102 (2000).
[50] J. L. Lyons, A. Janotti, and C. G. Van de Walle, J. Appl. Phys. **115**, 012014 (2014).
[51] A. D. Becke, J. Chem. Phys. **98**, 1372 (1993).
[52] J. P. Perdew, M. Ernzerhof, and K. Burke, J. Chem. Phys. **105**, 9982 (1996).
[53] A. Görling and M. Levy, J. Chem. Phys. **106**, 2675 (1997).
[54] J. Paier, M. Marsman, K. Hummer, G. Kresse, I. C. Gerber, and J. G. Ángyán, J. Chem. Phys. **124**, 154709 (2006).
[55] K. Biswas and M. H. Du, Phys. Rev. B **86**, 014102 (2012).
[56] J. Heyd, G. E. Scuseria, and M. Ernzerhof, J. Chem. Phys. **118**, 8207 (2003);
[57] P. Deák, B. Aradi, T. Frauenheim, E. Janzén, and A. Gali, Phys. Rev. B **81**, 153203 (2010).
[58] J. P. Perdew, W. Yang, K. Burke, Z. Yang, E. K. Gross, M. Scheffler, G. E. Scuseria, T. M. Henderson, I. Y. Zhang, A. Ruzsinszky, H. Peng, J. Sun, E. Trushin, and A. Görling, Proc. Natl. Acad. Sci. USA **114**, 2801 (2017).
[59] T. E. Peters and J. Baglio, J. Inorg. Nucl. Chem. **32**, 1089 (1970).
[60] B. V. Egorova, A. V. Olenev, P. S. Berdonosov, A. N. Kuznetsov, S. Y. Stefanovich, V. A. Dolgikh, T. Mahenthirarajah, and P. Lightfoot, J. Solid State Chem. **181**, 1891 (2008).
[61] V. P. Dotsenko, I. V. Berezovskaya, N. P. Efryushina, E. V. Shabanov, and A. S. Voloshinovskii, Phys. Status Solidi **203**, 892 (2006).
[62] A. V. Sidorenko, A. J. J. Bos, P. Dorenbos, P. A. Rodnyi, C. W. E. van Eijk, I. V. Berezovskaya, and V. P. Dotsenko, J. Phys.: Condens. Matter **15**, 3471 (2003).
[63] V. P. Dotsenko, I. V. Berezovskaya, N. P. Efryushina, A. S. Voloshinovskii, P. Dorenbos, and C. W. E. van Eijk, J. Lumin. **93**, 137 (2001).
[64] G. Bergerhoff, R. Hundt, R. Sievers, and I. D. Brown, J. Chem. Inf. Comp. Sci. **23**, 66 (1983).
[65] J. P. Perdew, K. Burke, and M. Ernzerhof, Phys. Rev. Lett. **77**, 3865 (1996).
[66] G. Kresse and J. Hafner, Phys. Rev. B **47**, 558 (1993).
[67] G. Kresse and J. Furthmüller, Phys. Rev. B **54**, 11169 (1996).
[68] G. Kresse and J. Furthmüller, Comput. Mater. Sci. **6**, 15 (1996).
[69] G. Kresse and D. Joubert, Phys. Rev. B **59**, 1758 (1999).
[70] P. E. Blöchl, Phys. Rev. B **50**, 17953 (1994).
[71] H. J. Monkhorst and J. D. Pack, Phys. Rev. B **13**, 5188 (1976).
[72] P. Blaha, K. Schwarz, G. K. H. Madsen, D. Kvasnicka, and J. Luitz, WIEN2K: An augmented plane wave + local orbitals

program for calculating crystal properties, Technische Universität, Vienna, 2001.
[73] A. D. Becke and E. R. Johnson, J. Chem. Phys. **124**, 221101 (2006).
[74] F. Tran and P. Blaha, Phys. Rev. Lett. **102**, 226401 (2009).
[75] D. Koller, F. Tran, and P. Blaha, Phys. Rev. B **85**, 155109 (2012).
[76] L. van Pieterson, M. F. Reid, R. T. Wegh, S. Soverna, and A. Meijerink, Phys. Rev. B **65**, 045113 (2002).
[77] L. van Pieterson, M. F. Reid, G. W. Burdick, and A. Meijerink, Phys. Rev. B **65**, 045114 (2002).
[78] T. Mattila and A. Zunger, Phys. Rev. B **58**, 1367 (1998).
[79] C. G. Van de Walle and J. Neugebauer, J. Appl. Phys. **95**, 3851 (2004).
[80] L. Ning, W. Cheng, C. Zhou, C. Duan, and Y. Zhang, J. Phys. Chem. C **118**, 19940 (2014).
[81] G. Makov and M. C. Payne, Phys. Rev. B **51**, 4014 (1995).
[82] S. Lany and A. Zunger, Phys. Rev. B **78**, 235104 (2008).
[83] K. F. Young and H. P. R. Frederikse, J. Phys. Chem. Ref. Data **2**, 313 (1973).
[84] M. Leslie and N. J. Gillan, J. Phys. C **18**, 973 (1985).
[85] A. Gelle and M. Lepetit, J. Chem. Phys. **128**, 244716 (2008).
[86] B. O. Roos, P. R. Taylor, and P. E. M. Siegbahn, Chem. Phys. **48**, 157 (1980).
[87] G. Karlström, R. Lindh, P. Å. Malmqvist, B. O. Roos, U. Ryde, V. Veryazov, P. O. Widmark, M. Cossi, B. Schimmelpfennig, P. Neogrady, and L. Seijo, Comput. Mater. Sci. **28**, 222 (2003).
[88] L. Seijo, Z. Barandiaran, and B. Ordejon, Mol. Phys. **101**, 73 (2003).
[89] Z. Barandiaran and L. Seijo, Can. J. Chem. **70**, 409 (1992).
[90] M. D. Lloyd, A. Levasseur, and C. Fouassier, J. Solid State Chem. **6**, 179 (1973).
[91] K. I. Machida, G. Y. Adachi, Y. Moriwaki, and J. Shiokawa, Bull. Chem. Soc. Jpn. **54**, 1048 (1981).
[92] V. P. Dotsenko, I. V. Berezovskaya, P. V. Pyrogenko, N. P. Efryushina, P. A. Rodnyi, C. W. E. Van Eijk, and A. V. Sidorenko, J. Solid State Chem. **166**, 271 (2002).
[93] Q. Jing, X. Dong, X. Chen, Z. Yang, S. Pan, and C. Lei, Chem. Phys. **453**, 42 (2015).
[94] N. E. Brese and M. O'keeffe, Acta Crystallogr. Sect. B **47**, 192 (1991).
[95] S. Poncé, Y. Jia, M. Giantomassi, M. Mikami, and X. Gonze, J. Phys. Chem. C **120**, 4040 (2016).
[96] P. Dorenbos, J. Phys.: Condens. Matter **17**, 8103 (2005).
[97] V. Fiorentini and A. Baldereschi, Phys. Rev. B **51**, 17196 (1995).
[98] M. A. L. Marques, J. Vidal, M. J. T. Oliveira, L. Reining, and S. Botti, Phys. Rev. B **83**, 035119 (2011).
[99] F. Viñes, O. Lamiel-García, K. Chul Ko, J. Yong Lee, and F. Illas, J. Comput. Chem. **38**, 781 (2017).
[100] P. Deák, Q. Duy Ho, F. Seemann, B. Aradi, M. Lorke, and T. Frauenheim, Phys. Rev. B **95**, 075208 (2017).
[101] S. Lany and A. Zunger, Phys. Rev. B **80**, 085202 (2009).